Nickel Ferrocyanide as High-Performance Next Generation Electrocatalyst for Urea Oxidation

Shi-Kui Geng
Anhui University
Yao Zheng
University of Adelaide https://orcid.org/0000-0002-2411-8041
Shan-Qing Li
Chizhou University
Xu Zhao
University of Science and Technology of China
Jun Hu
Anhui University
Hai-Bo Shu
Anhui University
Mietek Jaroniec
Department of Chemistry and Biochemistry https://orcid.org/0000-0002-1178-5611
Ping Chen
Anhui University
Qinghua Liu
University of Science and Technology of China https://orcid.org/0000-0003-4090-3311
Shizhang Qiao (s.qiao@adelaide.edu.au)
University of Adelaide https://orcid.org/0000-0002-4568-8422

Article

Keywords: nickel ferrocyanide, urea oxidation reaction, electrocatalyst

Posted Date: September 10th, 2020

DOI: https://doi.org/10.21203/rs.3.rs-67358/v1

Version of Record: A version of this preprint was published at Nature Energy on September 20th, 2021. See the published version at https://doi.org/10.1038/s41560-021-00899-2.

Abstract

Urea oxidation, a key process in energy and environmental science, faces challenges because of the insufficient understanding of its mechanism and the lack of efficient catalysts. Here we demonstrate that nickel ferrocyanide ($Ni_2Fe(CN)_6$) molecular catalyst supported on Ni form can drive urea oxidation reaction (UOR) with the record electrochemical activity and stability among all supported catalysts reported so far. A combination of kinetics data, in-situ spectroscopic measurements and energy computations suggests a new UOR pathway that delivers such outstanding performance. Different from most studied Ni-based catalysts with NiOOH derivative as a real catalytically active site for UOR, $Ni_2Fe(CN)_6$ appears to be a next-generation catalyst able to directly facilitate a two-step reaction pathway involving a critical reaction of intermediate ammonia's production (on Ni site) and oxidation (on Fe site). Due to the alternative rate-determining step with a more favorable thermal energetics, $Ni_2Fe(CN)_6$ broke the limiting activity of the reported so far UOR catalysts. As a result, the UOR process on $Ni_2Fe(CN)_6$ can replace conventional water oxidation process in various energy-saving systems for hydrogen and hydrogen peroxide production.

Introduction

Electrochemical urea oxidation reaction (UOR) is of great importance in a range of energy-related applications and devices.[1-5] Due to a more negative equilibrium potential (E^0 = 0.37 V *vs* reversible hydrogen electrode, RHE), UOR is an ideal alternative anode half reaction to conventional oxygen evolution reaction (OER, E^0 = 1.23 V *vs* RHE) for pure hydrogen and hydrogen peroxide production in energy-saving water electrolyzers.[6,7] Practically, compared to precious pure water oxidation and poisoning methanol/hydrazine oxidation reactions, UOR process has significant advantages because urea is globally abundant in human urine, urea-rich wastewater and byproduct of industrial activities. In addition, compared to the emerging seawater oxidation, UOR can avoid chlorine gas generation because of the lower reaction potential of UOR than that for chlorine evolution reaction (E^0 = 1.36 V *vs* RHE).[8] Therefore, using UOR to replace OER can not only save the energy input but also reduce the contamination of urea-rich wastewater.[4,6]

Compared to OER, UOR suffers from even more sluggish kinetics because of the complicated $6e^-$ transfer process, which needs high performance catalysts to decrease the overpotential to achieve an efficient device.[2, 9-11] Initially, some noble metal catalysts such as Ti-Pt, Ti-Pt-Ir, and Ru were used to enhance the activity, however due to their scarcity they are costly.[2] However, the catalytic performance of the recently developed non-noble metal UOR catalysts based on Ni hydroxides, oxides, sulfides, and phosphides, etc, does not satisfy requirements of practical applications due to the high overpotential, low current density and inadequate stability.[7,12,13] For example, the best so far Ni-based UOR catalysts, e.g., $Ni_{0.9}Fe_{0.1}O_x$, can deliver a 10 mA cm^{-2} at the potential of 1.34 V (*vs* RHE) in 1.0 M KOH with 0.33 M urea, which does not represent a significant improvement to the potential on as compared to the state-of-the-art OER

catalysts.[14] In addition, the stability of the reported UOR catalysts is questionable; only a few catalysts maintain a relative current density higher than 90 % of the initial value for 50 hour continuous reaction.[12]

This poor performance may be due to the inherent reaction mechanism. Specifically, for the most studied Ni-based materials, before UOR onset (e.g., 1.40 V *vs* RHE), the catalysts inevitably undergo a self-oxidation process to form Ni^{3+} stated NiOOH derivative on the surfaces (always happens at ~1.36 V *vs* RHE), which then serves as the direct active sites for UOR. Under this scheme, the rate-determining step (RDS) of the overall reaction is desorption of the last *COO intermediate from the active sites to form CO_3^{2-} in the electrolyte. However, because of a strong binding of Ni^{3+} active sites with *COO intermediate, the energetics (~1242.2 kJ mol^{-1}) for this reaction mechanism is unfavorable, which results in low activity of the catalyst.[15] In addition, this reaction pathway involves a CO intermediate, which can poison the catalysts and make them unstable.[2,15] Even though a wide variety of catalysts have been developed with different compositions and structures, most of them involve NiOOH species, which limits their activity (the best one is ~101 mA cm^{-2} at a potential of 1.40 V *vs* RHE in 1.0 M KOH with 0.33 M urea).[9,16,17] Note that as a $6e^-$ transfer reaction, the UOR process should have more alternatives with optimal thermodynamics or kinetics beyond the mechanism involving NiOOH species. This has been widely validated for other multiple-electron transfer reactions such as oxygen reduction reaction and carbon dioxide reduction reaction that have multiple reaction pathways.[18] One can image that a new mechanism with more rational reaction intermediates and better adsorption free energy can significantly improve the activity of catalysts.[12,18,19] This improvement can be achieved by employing the atomic-level design of high-performance UOR catalysts and by performing the advanced spectroscopic studies to identify the critical reaction intermediates.

In this work, we propose a new and more energetically favorable UOR pathway triggered by nickel ferrocyanide $Ni_2Fe(CN)_6$ electrocatalyst, one of Prussian blue analogues.[20] With an alternative reaction intermediate, the new reaction mechanism on $Ni_2Fe(CN)_6$ delivers one of the best UOR activity and assures high stability as compared to the existing catalysts. Through an advanced characterization by in-situ techniques (e.g., synchrotron radiation-Fourier transform infrared spectroscopy, Raman spectroscopy, ammonia detection) and density functional theory (DFT) computation, a critical intermediate of *NH_3 was identified, which involves two steps of production and oxidation of NH_3 on different sites of the catalyst surface. This mechanism is very different from the currently known mechanism with *NCO, *HN-CO or *COO as the key intermediates. In addition, our experiment demonstrated the UOR process driven by $Ni_2Fe(CN)_6$ can effectively replace the conventional water oxidation in different energy saving systems for hydrogen or H_2O_2 production.

Results And Discussion

Physicochemical properties. The typical $Ni_2Fe(CN)_6$ catalyst was prepared on nickel foam through a self-assembly method by immersing cleaned Ni foams in the mixed solution of polyvinylpyrrolidone,

$C_6H_5Na_3O_7 \cdot 2H_2O$, $NiCl_2 \cdot 6H_2O$ and $K_3[Fe(CN)]_6$ using different aging times and salt concentrations. Scanning electron microscope (SEM) image shows that the as-synthesized product is composed of nanocubes assembled on the surface of nickel foam with a single layer coating (Fig. 1a). Transmission electron microscope (TEM) image shows a highly crystalline cubic nanoparticle with an edge length of 180 ± 10 nm (Fig. 1a inset). Different reaction conditions can be used to tune the nanocube size and coverage on the nickel foam (Supplementary Fig. 1, 2). Analysis of the X-ray powder diffraction (XRD) pattern obtained for $Ni_2Fe(CN)_6$ powder (Fig. 1b) allowed for identification of a single cubic phase where Fe atom coordinates with carbon atoms in CN^- species and Ni atom has two coordination forms: one coordinates with N atoms in CN^- species and the other is situated in the center alone.[21,22] Interestingly, both Fe^{2+} and Ni^{2+} species were not oxidized during UOR process (Fig. 1c, d), which differs from the mechanism reported for other Ni-based catalysts. [9, 15]

UOR performance evaluation. Since human urine contains 2-2.5 wt. % of urea (equals to a molar concentration of ~ 0.33 M), 0.33 M urea was chosen in the electrolysis.[2, 12] As shown by the linear sweep voltammetry (LSV), UOR on an optimized $Ni_2Fe(CN)_6$ catalyst exhibits a more negative onset potential than that of OER (Fig. 2a, Supplementary Fig. 3). To obtain a current density of 100 mA cm^{-2}, UOR needs a potential of 1.35 V, much smaller than that for OER (1.68 V). More importantly, as shown in Fig. 2a, the urea oxidation on $Ni_2Fe(CN)_6$ proceeds before the self-oxidation of Ni^{2+} to Ni^{3+}. This is very different from the mechanism reported for other reported Ni-based catalysts, in which a NiOOH phase is formed before UOR and serves as the active sites.[15] Specifically, for $Ni_2Fe(CN)_6$ catalyst a very small apparent UOR activation energy of 14.0 kJ/mol (at a potential of 1.39 V) is observed (Supplementary Fig. 4). Importantly, the potential of 1.35 V to achieve an UOR current density of 100 mA·cm^{-2} on $Ni_2Fe(CN)_6$ is the lowest one among all known UOR electrocatalysts reported including nickel hydroxides, metals, phosphides, etc.[10,13,16,23–33] In addition, the current density at a certain potential (e.g. 1.40 V) on $Ni_2Fe(CN)_6$ is 2.5 times higher than that obtained for the state-of-the-art nickel-based supported electrocatalysts (Supplementary Fig. 5, Table 2).[14] Interestingly, it was also found that two other cyanides, ferric ferrocyanide ($Fe_4[Fe(CN)_6]_3$) and nickel cobaltcyanide ($Ni_3[Co(CN)_6]_2$), showed worse activity compared to $Ni_2Fe(CN)_6$ (Fig. 2b, Supplementary Fig. 6).[34,35] Therefore, we speculate that the observed high performance of $Ni_2Fe(CN)_6$ is caused by cooperative action of two active sites of Ni and Fe in $Ni_2Fe(CN)_6$ catalyst.

The kinetic study shows that the UOR process on $Ni_2Fe(CN)_6$ is independent of urea concentration (Fig. 2c), which agrees with the reported so far Ni-based electrocatalysts.[36] As can be seen in Fig. 2d, UOR shows a strong dependence on the amount of KOH with a reaction order of 1.10 to OH^- concentration, which is different from that of about 2.00 for other Ni-based electrocatalysts.[36] For example, a reaction order of 1.75 was obtained on a conventional UOR catalyst of NiC_2O_4 (Supplementary Fig. 7,8).[37] It was revealed that the UOR's RDS on NiOOH intermediated electrocatalysts is desorption of CO_2 from NiOOH [illegible] electrolyte. [15, 38–40] Therefore, the reaction

order of 1.10 on the newly developed $Ni_2Fe(CN)_6$ catalyst indicates an alternative reaction pathway and RDS.

Comparison to the conventional NiC_2O_4 catalyst. The above statement was validated by in-situ Raman spectroscopy studies of two types of catalysts, $Ni_2Fe(CN)_6$ and conventional NiC_2O_4 (Supplementary Fig. 9). As shown in Fig. 3a, two strong peaks at 2100 and 2140 cm^{-1} are characteristic of cyanide stretching in $Ni_2Fe(CN)_6$ complex,[20] while the peaks at 250 and 348 cm^{-1} belong to the Ni-N stretching vibration and the peak at 510 cm^{-1} belongs to the Fe-C stretching vibration, respectively.[22] Importantly, at various potentials and different reaction times (Fig. 3a, Supplementary Fig. 10a), the Raman spectra of $Ni_2Fe(CN)_6$ are similar to that at the open circuit potential (OCP). However, for NiC_2O_4, the NiOOH doublet peaks at 473 and 560 cm^{-1} appear in a very short time at a high potential during UOR process (Fig. 3b and Supplementary Fig. 10b), indicating it is partially reconstructed to NiOOH, which serves as the active phase for UOR and agrees with the existing literature.[38,39] As expected, $Ni_2Fe(CN)_6$ without NiOOH species showed a significantly enhanced apparent UOR activity and stability compared to NiC_2O_4 catalyst (Fig. 3c). About 90% of the current density remained after 50 hour operation on $Ni_2Fe(CN)_6$, which is a record for UOR catalysts.

The new reaction pathway of UOR for $Ni_2Fe(CN)_6$ was further investigated by the real-time ammonia detection in the electrolyte using an ion ammonia-selective electrode (Orion™ High-Performance Ammonia Electrode 9512HPBNWP, Supplementary Fig. 11).[41–43] As shown in Fig. 3d, a large amount of ammonia was produced and detected on $Ni_2Fe(CN)_6$ under a potential of 1.36 V (current density of 70.0 mA cm^{-2}), while very little was detected on NiC_2O_4 at similar conditions (current density of 72.0 mA cm^{-2} at a potential of 1.45 V). It was further found that $Ni_2Fe(CN)_6$ also can efficiently catalyze the oxidation of ammonia (Supplementary Fig. 12). Therefore, we propose that the UOR process on $Ni_2Fe(CN)_6$ contains $*NH_3$ as a key reaction intermediate, which is very different from the currently reported mechanisms involving *NCO, *HN-CO, or *COO as the intermediates.[38,39]

DFT computations. Based on the above analysis of kinetics and real-time ammonia detection, we propose a new mechanism for UOR, which comprises of two steps, namely production of NH_3 and oxidation of NH_3 (the detailed pathways can be found in the experimental section). The Gibbs free energy of each reaction intermediate was computed by density functional theory (DFT, Supplementary Table 1 and Supplementary Figs. 13–16). For the first step (Fig. 4a), Ni sites were proven to be the primary active sites because the free energy value of RDS ($[M{\cdot}OCO_2]_{ads} + 2e^- \rightarrow M + CO_3^{2-}$) on Ni site is smaller than that on Fe site. For the second step (Fig. 4b), the biggest difference is in the formation of $*NH{\cdot}NH_2$ intermediates, which reveals that the dehydrogenation reaction ($[M{\cdot}NH_2{\cdot}NH_2]_{ads} + OH^- \rightarrow [M{\cdot}NH{\cdot}NH_2]_{ads} + H_2O + e^-$) is harder to occur on Ni sites than Fe sites (free energy of 1.23 *vs* 0.94 eV). For the overall reaction pathways, the calculated RDS is the formation of $*NH + * NH_2$ (IMFe9 to IMFe10 as shown in Fig. 4b), in which 1 M $*NH_2$ + $*NH_2$ react with 1 M OH^-, which yields the reaction order of 1.0 with respect

to the OH^- concentration. This result agrees well with the experimentally determined reaction order of 1.10 on $Ni_2Fe(CN)_6$ catalyst (Fig. 2d). Overall, it is proposed that Ni is responsible for conversion of urea into ammonia and carbonate, while Fe is responsible for transformation of ammonia into nitrogen (Fig. 4c). This synergistic catalysis between Ni and Fe sites revealed by DFT computation agrees well with experimental observation that $Ni_2Fe(CN)_6$ exhibits remarkably higher activity than other two types of $Fe_4[Fe(CN)_6]_3$ and $Ni_3[Co(CN)_6]_2$ catalysts (Fig. 2b).

Identification of intermediates. We performed in-situ synchrotron radiation-Fourier transform infrared spectroscopy (SR-FTIR) analysis to identify the critical reaction intermediates proposed in the DFT computation and real-time ammonia detection. As shown in Fig. 5a, compared with the spectrum at OCP, two obvious absorption bands appear at 2925 cm^{-1} and 1203 cm^{-1} under the UOR working potential (e.g. 1.35–1.65 V), which can be assigned to the N-H stretching vibration of $*N = NH_2^+$ and C-O stretching vibration of $*OCONH_2$ species, respectively.[44, 45] In addition, with increasing potential and operating time, these two characteristic peaks become stronger (Fig. 5b-c and Supplementary Fig. 17). The simulated results of harmonic vibrational frequencies (Fig. 5d) also indicate that two peaks can be attributed to $*N = NH_2^+$ and $*OCONH_2$ species. This clearly indicates that these two intermediates are produced in the UOR process, which supports the DFT computation with IMFe12 and IMNi3 intermediates. At this stage, the combination of kinetics analysis, DFT computation and in-situ SR-FTIR spectroscopy data confirms a new UOR mechanism on $Ni_2Fe(CN)_6$ without NiOOH generation, namely two-step processes of NH_3 production and oxidation at two different active sites.

Energy-saving systems driven by UOR for replacement of OER. To establish an energy-saving system benefiting from the low overpotential of UOR on $Ni_2Fe(CN)_6$ catalyst, we assembled an UOR//HER electrolyzer using $Ni_2Fe(CN)_6$ as the anode in an electrolyte containing 1 M KOH and 0.33 M urea. For comparison, an OER//HER electrolyzer with RuO_2 as the anode for OER was performed in 1.0 M KOH (Supplementary Fig. 18). To obtain a current density of 10 and 100 mA cm^{-2}, urea electrolysis needs a cell voltage of 1.38 and 1.50 V, respectively, whereas water electrolysis needs the value of 1.56 and 1.85 V (Fig. 6a). This clearly indicates the energy-saving advantage of the UOR process on $Ni_2Fe(CN)_6$ electrocatalyst to replace OER. In addition, the H_2 production in this UOR//HER cell was very stable with a Faradaic efficiency higher than 90% (Fig. 6b, Supplementary Fig. 19). Besides H_2 production, the energy-saving system can also be applied in a UOR//$2e^-$ORR flow cell composed of $Ni_2Fe(CN)_6$ anode and mesoporous carbon (CMK-3) cathode [46] (Supplementary Fig. 20). Nowadays, in-situ electrochemical production of H_2O_2 via $2e^-$ ORR has become a promising way because it can reduce the danger and costs of the transportation of H_2O_2.[46, 47] As expected, the urea electrolysis needs a smaller energy input than water electrolysis for urea elimination and H_2O_2 generation (Supplementary Fig. 21). Specifically, a H_2O_2 production rate of 225.3 g $m^{-2}h^{-1}$ (with a Faradaic efficiency of 82.3%) and an urea elimination rate of 140.1 g $m^{-2}h^{-1}$ (with a Faradaic efficiency of 94.9%) were achieved at the cell voltage of only 0.62 V (Fig. 6c, Supplementary Fig. 22). In addition, the urea elimination and H_2O_2 generation were very

efficient for urea concentrations varying from 0.0033 to 0.33 M (Fig. 6d, Supplementary Fig. 23), which is in the range of industrial urea-containing wastewater.

Conclusions

In summary, $Ni_2Fe(CN)_6$ as a next-generation UOR electrocatalyst with excellent efficiency and stability was developed by a simple and readily scalable method. Studies of mechanism by employing the advanced *in situ* Raman spectroscopy, *in situ* SR-FTIR techniques and real-time ammonia detection revealed a new and more energetically favorable UOR pathway on $Ni_2Fe(CN)_6$ as compared to most reported electrocatalysts. DFT results revealed that the highly enhanced electrochemical performance originates from the synergistic effect of Ni and Fe double active sites in $Ni_2Fe(CN)_6$. The efficient UOR on $Ni_2Fe(CN)_6$ replacing conventional OER is advantageous because of energy saving and reducing contamination of urea-rich wastewater. This work opens a new avenue to develop alternative electrocatalysts for UOR with boosted activity and stability.

Methods

$Ni_2Fe(CN)_6$ synthesis. 0.1 mmol of polyvinylpyrrolidone (PVP), 1.5 mmol of $NiCl_2{\cdot}6H_2O$ and 2.1 mmol of $C_6H_5Na_3O_7{\cdot}2H_2O$ were dissolved in 300 mL of deionized water. Then the mixed solution was added dropwise to 200 mL of solution containing 0.5 mmol of $K_3[Fe(CN)_6]$. Ni foam was sonicated in acetone, diluted nitric acid solution and deionized water for 15 minutes, respectively. The cleaned Ni foam was placed into the mixed solution and aged for 48 hours to obtain the final $Ni_2Fe(CN)_6$ electrocatalyst.

Electrochemical measurements. IM6e electrochemical workstation (Zahner-Electrik, Germany) was used to test the UOR activity in a three-electrode system, in which the as-prepared free standing electrocatalyst was directly used as the working electrode. Hg/HgO electrode and carbon rod were used as the reference and counter electrodes, respectively. 1.0 M KOH was used as the electrolyte with 0.33 M urea. The LSV curves were obtained at a scan rate of 5 mV s^{-1}. All curves were corrected manually with iR compensation and the potential was converted to RHE. The UOR//HER system was carried out in a two-electrode mode separated by an anion membrane. The UOR//2e-ORR system was carried out in a commercial flow cell, in which the prepared $Ni_2Fe(CN)_6$ on nickel foam was used as the anode, and the mesoporous carbon coated gas diffusion electrode was used as the cathode.[46] The anode contained 1.0 mol L^{-1} KOH with 0.0033-0.33 mol L^{-1} urea and the cathode contained 1.0 mol L^{-1} KOH. The areas of anode and cathode are both 4 cm^2.

Electrochemical in situ Raman measurements. The Raman spectroscopy was carried out using a Via-Reflex spectrometer (Renishaw) with a laser excitation wavelength of 532 nm and the measured potential for UOR was in the range of 1.2–1.6 V controlled by an electrochemical workstation (CHI750E Instruments). The in-situ electrochemical three-electrode cell contained $Ni_2Fe(CN)_6$ electrocatalyst as the working electrode, Ag/AgCl as the reference electrode and Pt wire as the counter electrode. 1.0 M KOH

was used as the electrolyte with 0.33 M urea solution. All Raman spectra at various applied potentials were obtained after a constant potential was applied to the catalyst's electrode for 20 min.

In situ synchrotron radiation FTIR measurements. In situ SR-FTIR measurements were made at the infrared beamline BL01B of National Synchrotron Radiation Laboratory (NSRL, China) through a homemade top-plate cell reflection IR setup with a ZnSe crystal as the infrared transmission window (cutoff energy of ~ 625 cm^{-1}).[48] This end-station was equipped with an FTIR spectrometer (Bruker 66v/s) with a KBr beam splitter and liquid nitrogen cooled MCT detector. The system is coupled with an IR microscope (Bruker Hyperion 3000) with a 16x objective. It is capable to perform infrared spectroscopy measurements over a broad range of 15–4000 cm^{-1} with high spectral resolution of 0.25 cm^{-1}. The catalyst electrode is tightly pressed against the ZnSe crystal window with a micron-scale gap in order to reduce the loss of infrared light. To ensure the quality of the obtained SR-FTIR spectra, the apparatus adopts a reflection mode with a vertical incidence of infrared light. Each infrared absorption spectrum was acquired by averaging 514 scans at are solution of 2 cm^{-1}. All infrared spectra were obtained after a constant potential was applied to the catalyst's electrode for 30 min.

DFT calculations. Spin-polarized DFT calculations were carried out using the DMol3 quantum chemical module.[49,50] The gradient-corrected density-functional PW91 (Perdew-Wang generalized-gradient approximation) was applied to predict the structures, single-point energies, zero-point energies, as well as thermodynamic parameters.[51] The Tkatchenko-Scheffler term of semiempirical dispersion-correction for DFT (DFT-D) was considered to estimate the bond energy of the σ-π coordination between Ni^{2+} and CN^{-}.[52] Infrared spectra of active intermediates were derived from harmonic vibrational frequencies calculations[53], and the vibrational analysis was performed at the final geometry using the identical parameters with the geometry optimizations. More details on the DFT calculations are provided in Supporting Information.

Gibbs free energy changes of reactions were calculated as follows.

$$\Delta G = \Delta E + \Delta ZPE + \Delta \int_0^T C_p dT - T\Delta S + \Delta E_{sol}$$

where E is single-point energy, ZPE means zero-point energy, $\Delta \int_0^T C_p dT$ and $-T\Delta S$ stand for the correction factors of enthalpy and entropy, E_{sol} is the solvation energy. A new reaction mechanism comprised of two steps, namely the production of NH_3 and oxidation of NH_3, is proposed:

Step 1: Production of NH_3

$$M + CO(NH_2)_2 \rightarrow [M{\cdot}CO(NH_2)_2]_{ads}$$
$$[M{\cdot}CO(NH_2)_2]_{ads} + OH^- \rightarrow [M{\cdot}(OH){\cdot}CO(NH_2)_2]_{ads} + e^-$$
$$[M{\cdot}(OH){\cdot}CO(NH_2)_2]_{ads} \rightarrow [M{\cdot}OCONH_2]_{ads} + NH_3$$
$$[M{\cdot}OCONH_2]_{ads} + OH^- \rightarrow [M{\cdot}(OH){\cdot}OCONH_2]_{ads} + e^-$$
$$[M{\cdot}(OH){\cdot}OCONH_2]_{ads} \rightarrow [M{\cdot}OCO_2]_{ads} + NH_3$$
$$[M{\cdot}OCO_2]_{ads} + 2e^- \rightarrow M + CO_3^{2-}$$

Step 2: Oxidation of NH_3

$$M + NH_3 \rightarrow [M{\cdot}NH_3]_{ads}$$
$$[M{\cdot}NH_3]_{ads} + OH^- \rightarrow [M{\cdot}NH_2]_{ads} + H_2O + e^-$$
$$[M{\cdot}NH_2]_{ads} + NH_3 \rightarrow [M{\cdot}NH_2{\cdot}NH_3]_{ads}$$
$$[M{\cdot}NH_2{\cdot}NH_3]_{ads} + OH^- \rightarrow [M{\cdot}NH_2{\cdot}NH_2]_{ads} + H_2O + e^-$$
$$[M{\cdot}NH_2{\cdot}NH_2]_{ads} + OH^- \rightarrow [M{\cdot}NH{\cdot}NH_2]_{ads} + H_2O + e^-$$
$$[M{\cdot}NH{\cdot}NH_2]_{ads} \rightarrow [M{\cdot}NHNH_2]_{ads}$$
$$[M{\cdot}NHNH_2]_{ads} + OH^- \rightarrow [M{\cdot}NNH_2]_{ads} + H_2O + e^-$$
$$[M{\cdot}NNH_2]_{ads} + OH^- \rightarrow [M{\cdot}NNH]_{ads} + H_2O + e^-$$
$$[M{\cdot}NNH]_{ads} + OH^- \rightarrow M + N_2 + H_2O + e^-$$

Declarations

Competing Interests

The authors declare no competing interests.

Authors' contribution

P.C. and Y.Z. conceived the project. S.Z.Q. supervised the project. S.K.G. performed the experiments of materials preparation, characterizations and activity tests, with the assistance of J.H. and H.B.S. X.Z. and Q.H.L. performed the in-situ SR-FTIR tests. S.Q.L. performed DFT calculations. P.C., Y.Z. and S.Z.Q. wrote the manuscript. M. J. revised the manuscript.

Acknowledgements

We acknowledge the funding from National Natural Science Foundation of China (21771002, U1932212), (KJ2019A0861) and Australian Research

Council (DP160104866, FL170100154 and DP190103472).

References

1. Senthilkumar, N., Gnana kumar, G., Manthiram, A., 3D hierarchical core–shell nanostructured arrays on carbon fibers as catalysts for direct urea fuel cells. *Adv. Energy Mater.* **8**, 1702207 (2018).
2. Ye, K., Wang, G., Cao, D., Wang, G., Recent advances in the electro-oxidation of urea for direct urea fuel cell and urea electrolysis. *Top. Curr. Chem.* **376**, 42 (2018).
3. Sayed, E. T., et al., Direct urea fuel cells: Challenges and opportunities. *J. Power Sources* **417**, 159–175 (2019).
4. Yao, S. J., Wolfson, S. K., Ahn, B. K., Liu, C. C., Anodic oxidation of urea and an electrochemical approach to de-ureation. *Nature* **241**, 471–472 (1973).
5. Wester, M., et al., Removal of urea in a wearable dialysis device: A reappraisal of electro-oxidation. *Artif. Organs* **38**, 998–1006 (2014).
6. Yu, Z.-Y., et al., Ni–Mo–O nanorod-derived composite catalysts for efficient alkaline water-to-hydrogen conversion via urea electrolysis. *Energ. Environ. Sci.* **11**, 1890–1897 (2018).
7. Zhang, J.-Y., et al., Energy-saving hydrogen production coupling urea oxidation over a bifunctional nickel-molybdenum nanotube array. *Nano Energy* **60**, 894–902 (2019).
8. Yu, L., et al., Non-noble metal-nitride based electrocatalysts for high-performance alkaline seawater electrolysis. *Nat. Commun.* **10**, 5106 (2019).
9. Zhang, L., et al., A lattice-oxygen-involved reaction pathway to boost urea oxidation. *Angew. Chem. Int. Edit.* **58**, 16820–16825 (2019).
10. Chen, S., Duan, J., Vasileff, A., Qiao, S. Z., Size fractionation of two-dimensional sub-nanometer thin manganese dioxide crystals towards superior urea electrocatalytic conversion. *Angew. Chem. Int. Edit.* **55**, 3804–3808 (2016).
11. Zhu, X., et al., Metallic nickel hydroxide nanosheets give superior electrocatalytic oxidation of urea for fuel cells. *Angew. Chem. Int. Edit.* **55**, 12465–12469 (2016).
12. Zhu, B. J., Liang, Z. B., Zou, R. Q., Designing advanced catalysts for energy conversion based on urea oxidation reaction. *Small* **16**, 1906133 (2020).
13. Ding, Y., et al., Atomically thick $Ni(OH)_2$ nanomeshes for urea electrooxidation. *Nanoscale* **11**, 1058–1064.(2019).
14. Wu, F. C., et al., Bifunctional nickel oxide-based nanosheets for highly efficient overall urea splitting. *Chem. Commun.* **55**, 6555–6558 (2019).
15. Daramola, D. A., Singh, D., Botte, G. G., Dissociation rates of urea in the presence of NiOOH Catalyst: A DFT analysis. *J. Phys. Chem. A* **114**, 11513–11521 (2010).
16. Xie, J., et al., Copper-incorporated hierarchical wire-on-sheet α-$Ni(OH)_2$ nanoarrays as robust trifunctional catalysts for synergistic hydrogen generation and urea oxidation. *J. Mater. Chem. A* **7**,

13577–13584 (2019).

17. Forslund, R. P., Alexander, C. T., Abakumov, A. M., Johnston, K. P., Stevenson, K. J., Enhanced electrocatalytic activities by substitutional tuning of nickel-based ruddlesden–popper catalysts for the oxidation of urea and small alcohols. *ACS Catal.* **9**, 2664–2673 (2019).
18. Seh, Z. W., et al., Combining theory and experiment in electrocatalysis: Insights into materials design. *Science* **355**, eaad4998 (2017).
19. Jiao, Y., Zheng, Y., Chen, P., Jaroniec, M., Qiao, S. Z., Molecular scaffolding strategy with synergistic active centers to facilitate electrocatalytic CO_2 reduction to hydrocarbon/alcohol. *J. Am. Chem. Soc.* **139**, 18093–18100 (2017).
20. Simonov, A., et al., Hidden diversity of vacancy networks in Prussian blue analogues. *Nature.* **578**, 257–260 (2020).
21. Wang, X. W., Cheng, L., Multifunctional Prussian blue-based nanomaterials: Preparation, modification, and theranostic applications. *Coordin. Chem. Rev.* 419, 213393 (2020).
22. Steen, W. A., Jeerage, K. M., Schwartz, D. T., Raman spectroscopy of redox activity in cathodically electrodeposited nickel hexacyanoferrate thin films. *Appl. Spectrosc.* **56**, 1021–1029 (2002).
23. Zhang, J. Y., et al., Energy-saving hydrogen production coupling urea oxidation over a bifunctional nickel-molybdenum nanotube array. *Nano Energy* **60**, 894–902 (2019).
24. Zhu, D., et al., Two-dimensional metal–organic frameworks with high oxidation states for efficient electrocatalytic urea oxidation. *Chem. Commun.* **53**, 10906–10909 (2017).
25. Liu, D., et al., High-performance urea electrolysis towards less energy-intensive electrochemical hydrogen production using a bifunctional catalyst electrode. *J. Mater. Chem. A* **5**, 3208–3213 (2017).
26. Hu, S., et al., Ni_3N/NF as bifunctional catalysts for both hydrogen generation and urea decomposition. *Acs Appl. Mater. Inter.* **11**, 13168–13175 (2019).
27. Sha, L., et al., The construction of self- supported thorny leaf- like nickel-cobalt bimetal phosphides as efficient bifunctional electrocatalysts for urea electrolysis. *J. Mater. Chem. A* **7**, 9078–9085 (2019).
28. Yan, L., et al., Facile in-situ growth of Ni_2P/Fe_2P nanohybrids on Ni foam for highly efficient urea electrolysis. *J. Colloid Interf. Sci.* **541**, 279–286 (2019).
29. Li, Y. J., Wang, H. W., Wang, R., He, B. B., Gong, Y. S., 3D self-supported Fe-O-P film on nickel foam as a highly active bifunctional electrocatalyst for urea-assisted overall water splitting. *Mater. Res. Bull.* **100**, 72–75 (2018).
30. Liu, Q., et al., A porous Ni_3N nanosheet array as a high-performance non-noble-metal catalyst for urea-assisted electrochemical hydrogen production. *Inorg. Chem. Front.* **4**, 1120–1124 (2017).
31. Xiao, C. L., Li, S. N., Zhang, X. Y., MacFarlane, D. R., $MnO_2/MnCo_2O_4$/Ni heterostructure with quadruple hierarchy: a bifunctional electrode architecture for overall urea oxidation. *J. Mater. Chem. A* **5**, 7825–7832 (2017).

32. Wu, M. S., Sie, Y. J., Yang, S. B., Hollow mesoporous nickel dendrites grown on porous nickel foam for electrochemical oxidation of urea. *Electrochim. Acta* **304**, 131–137 (2019).
33. Zequine, C., et al., Nanosheets of $CuCo_2O_4$ As a High-performance electrocatalyst in urea oxidation. *Appl. Sci.-Basel* **9**, 793 (2019).
34. Hu, M., Ishihara, S., Ariga, K., Imura, M., Yamauchi, Y., Kinetically controlled crystallization for synthesis of monodispersed coordination polymer nanocubes and their self-assembly to periodic arrangements. *Chem. Eur. J.* **19**, 1882–1885 (2013).
35. Zhang, W., et al., Prussian blue nanoparticles as multienzyme mimetics and reactive oxygen species scavengers. *J. Am. Chem. Soc.* **138**, 5860–5865 (2016).
36. Vedharathinam, V., Botte, G. G., Understanding the electro-catalytic oxidation mechanism of urea on nickel electrodes in alkaline medium. *Electrochim. Acta* **81**, 292–300 (2012).
37. Garcia-Clavel, M. E., Martinez-Lope, M. J., Casais-Alvarez, M. T., Thermal study of $NiC_2O_4 \cdot 2H_2O$ obtained by a solid state reaction at room temperature and normal pressure. *Thermochim. Acta* **118**, 123–134 (1987).
38. Vedharathinam, V., Botte, G. G., Direct evidence of the mechanism for the electro-oxidation of urea on Ni(OH)(2) catalyst in alkaline medium. *Electrochim. Acta* **108**, 660–665 (2013).
39. Vedharathinam, V., Botte, G. G., Experimental investigation of potential oscillations during the electrocatalytic oxidation of urea on Ni catalyst in alkaline medium. *J. Phys. Chem. C* **118**, 21806–21812 (2014).
40. Tang, C., et al., Se-Ni(OH)(2)-shelled vertically oriented NiSe nanowires as a superior electrocatalyst toward urea oxidation reaction of fuel cells. *Electrochim. Acta* **248**, 243–249 (2017).
41. Chen, S., et al., Electrocatalytic synthesis of ammonia at room temperature and atmospheric pressure from water and nitrogen on a carbon-nanotube-based electrocatalyst. *Angew. Chem. Int. Edit.* **56**, 2699–2703 (2017).
42. American Public Health Association (APHA)
Federation, W. E., Association, A. P. H., American Public Health Association (APHA): Washington, DC, USA 2005.
43. Wen, Y. Z., Mao, Y. F., Kang, Z. F., Luo, Q. H., Application of an ammonium ion-selective electrode for the real-time measurement of ammonia nitrogen based on pH and temperature compensation. *Measurement* **137**, 98–101 (2019).
44. Nakamoto, K., Infrared and Raman spectra of inorganic and coordination compounds. *Handbook of vibrational spectroscopy*, 2006, *New York: John Wiley & Sons, Ltd.*
45. Griffiths, P., De Haseth, J., Winefordner, J., *Fourier transform infrared spectrometry*, 1986, *New York: John Wiley & Sons, Ltd.*
46. Wang, Y.-L., et al., One minute from pristine carbon to an electrocatalyst for hydrogen peroxide production. *J. Mater. Chem. A* **7**, 21329–21337 (2019).

47. Lu, Z., et al., High-efficiency oxygen reduction to hydrogen peroxide catalysed by oxidized carbon materials. *Nat. Catal.* **1**, 156–162 (2018).
48. Cheng, W., et al., Lattice-strained metal–organic-framework arrays for bifunctional oxygen electrocatalysis. *Nat. Energy* **4**, 115–122 (2019).
49. Delley, B., An all-electron numerical method for solving the local density functional for polyatomic molecules. *J. Chem. Phys.* **92**, 508–517 (1990).
50. Delley, B., From molecules to solids with the DMol3 approach. *J. Chem. Phys.* **113**, 7756–7764 (2000).
51. Perdew, J. P., Wang, Y., Accurate and simple analytic representation of the electron-gas correlation energy. *Phys. Rev. B* **45**, 13244–13249 (1992).
52. Tkatchenko, A., Scheffler, M., Accurate molecular van der waals interactions from ground-state electron density and free-atom reference data. *Phys. Rev. Lett.* **102**, 073005 (2009).
53. Allis, D. G., Prokhorova, D. A., Korter, T. M., Solid-state modeling of the terahertz spectrum of the high explosive HMX. *J. Phys. Chem. A* **110**, 1951–1959 (2006).

Figures

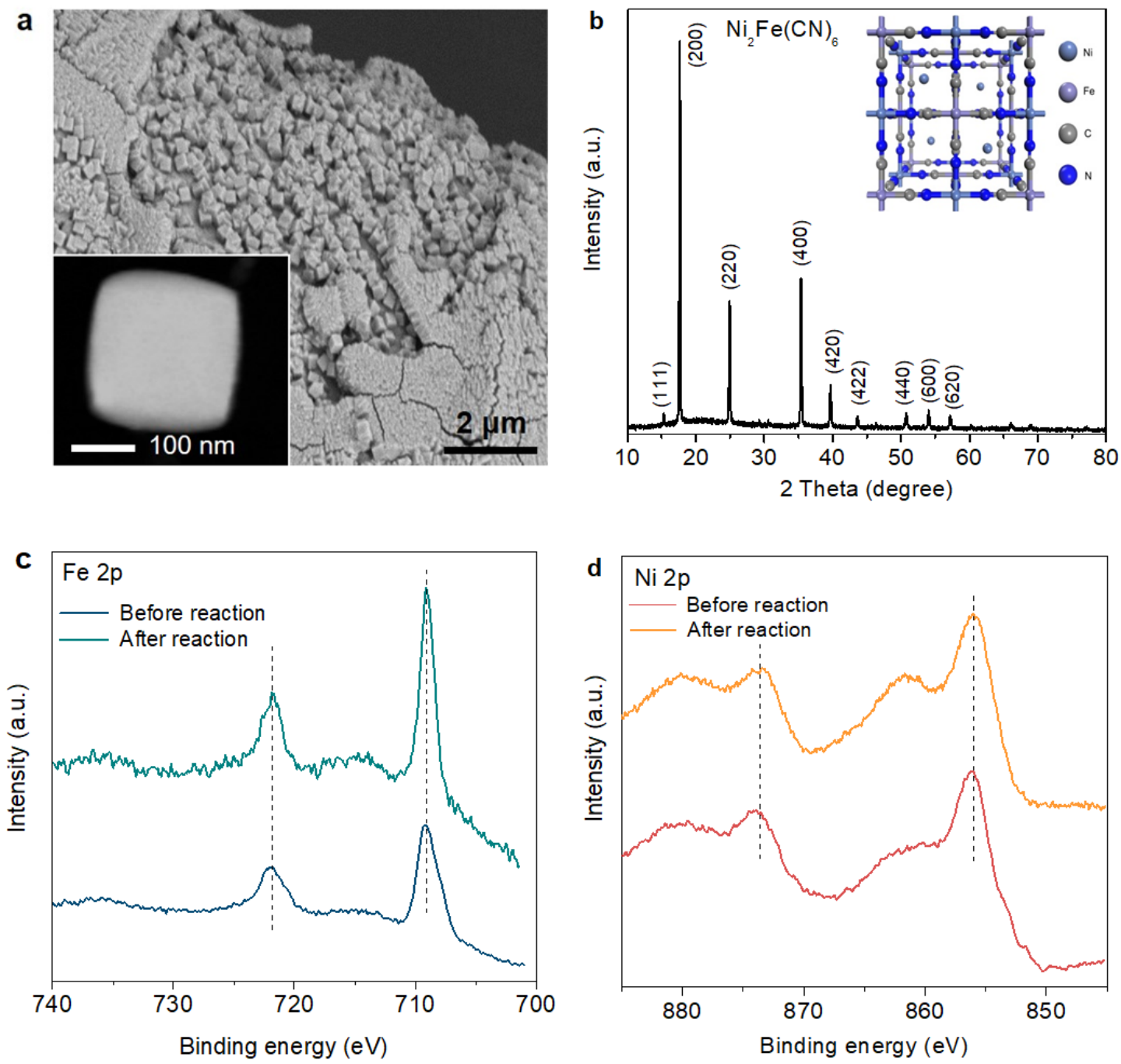

Figure 1

Physicochemical characterization of Ni2Fe(CN)6 catalyst. a, SEM and TEM (inset) images of freshly synthesized catalyst. b, XRD pattern with indexed peaks of freshly synthesized catalyst and the schematic illustration of the catalyst (inset). c, d, High resolution Fe 2p and Ni 2p XPS spectra of Ni2Fe(CN)6 before and after UOR tests.

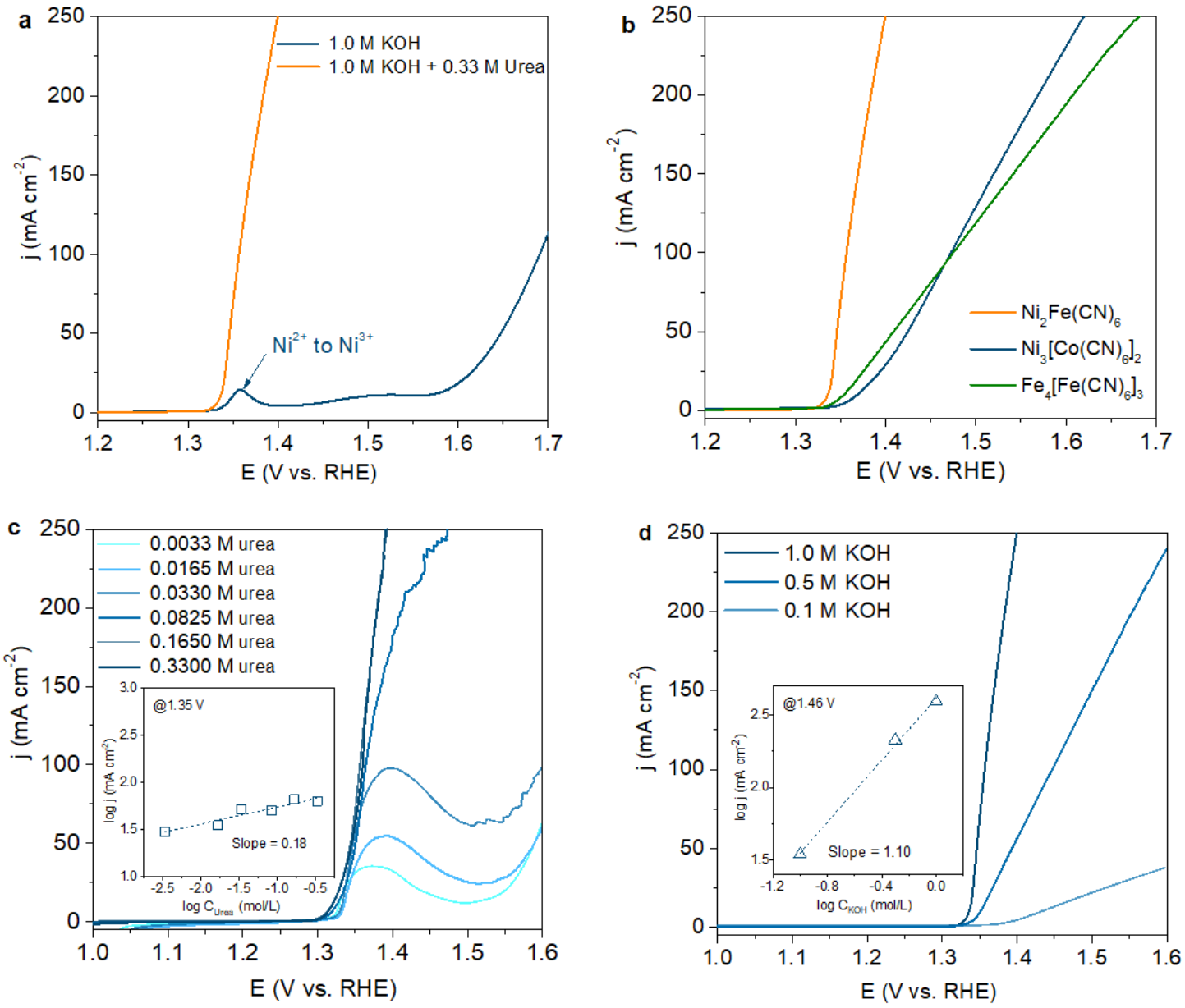

Figure 2

Evaluation of the UOR performance on Ni2Fe(CN)6 catalyst in a three-electrode cell. a, LSV curves of electrode in different electrolytes. The arrow shows the electrochemical oxidation of nickel ion on the catalyst. b, LSV curves of various catalysts in 1.0 M KOH containing 0.33 M urea. c, LSV curves of Ni2Fe(CN)6 in 1.0 M KOH electrolytes with different concentrations of urea. Inset shows the dependence of the UOR current density on the urea concentration at 1.35 V vs RHE. d, LSV curves of Ni2Fe(CN)6 at different concentrations of KOH electrolyte containing 0.33 M urea. Inset shows the dependence of the UOR current density on the KOH concentration at 1.46 V vs RHE.

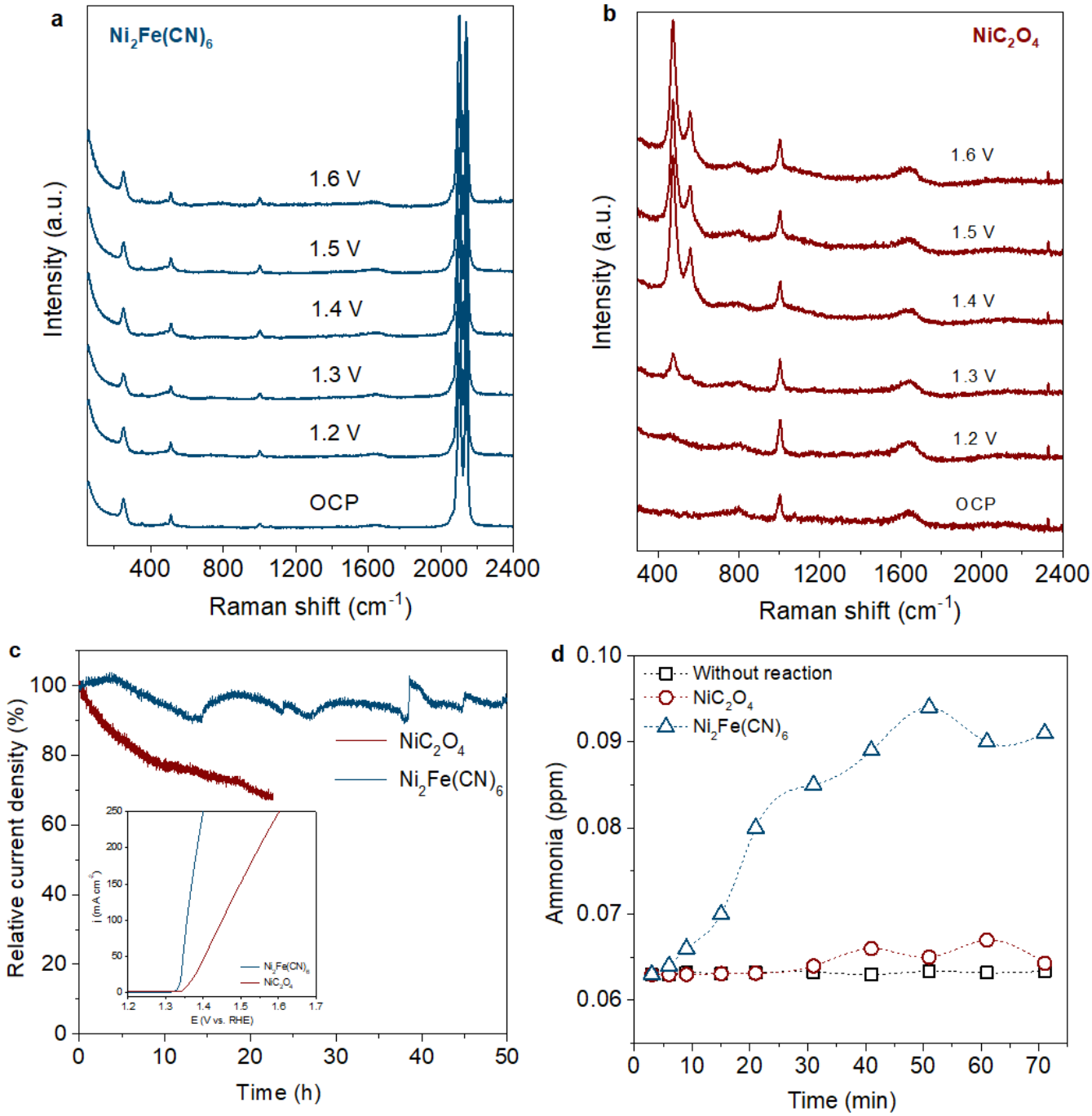

Figure 3

Comparison of Ni2Fe(CN)6 and conventional NiC2O4 catalysts. a, b, In-situ Raman spectra in 1.0 M KOH with 0.33 M urea at various applied potentials. c, Relative current density from the amperometric i-t curves obtained for Ni2Fe(CN)6 (at a potential of 1.34 V vs RHE) and NiC2O4 (at a potential of 1.41 V vs RHE) catalysts in 1.0 M KOH with 0.33 M urea and LSV curves (inset). d, Ammonia concentration measured in a three-electrode system in 1.0 M KOH with 0.033 M urea for Ni2Fe(CN)6 (at a potential of 1.36 V vs RHE) and NiC2O4 catalysts (at a potential of 1.45 V vs RHE), respectively.

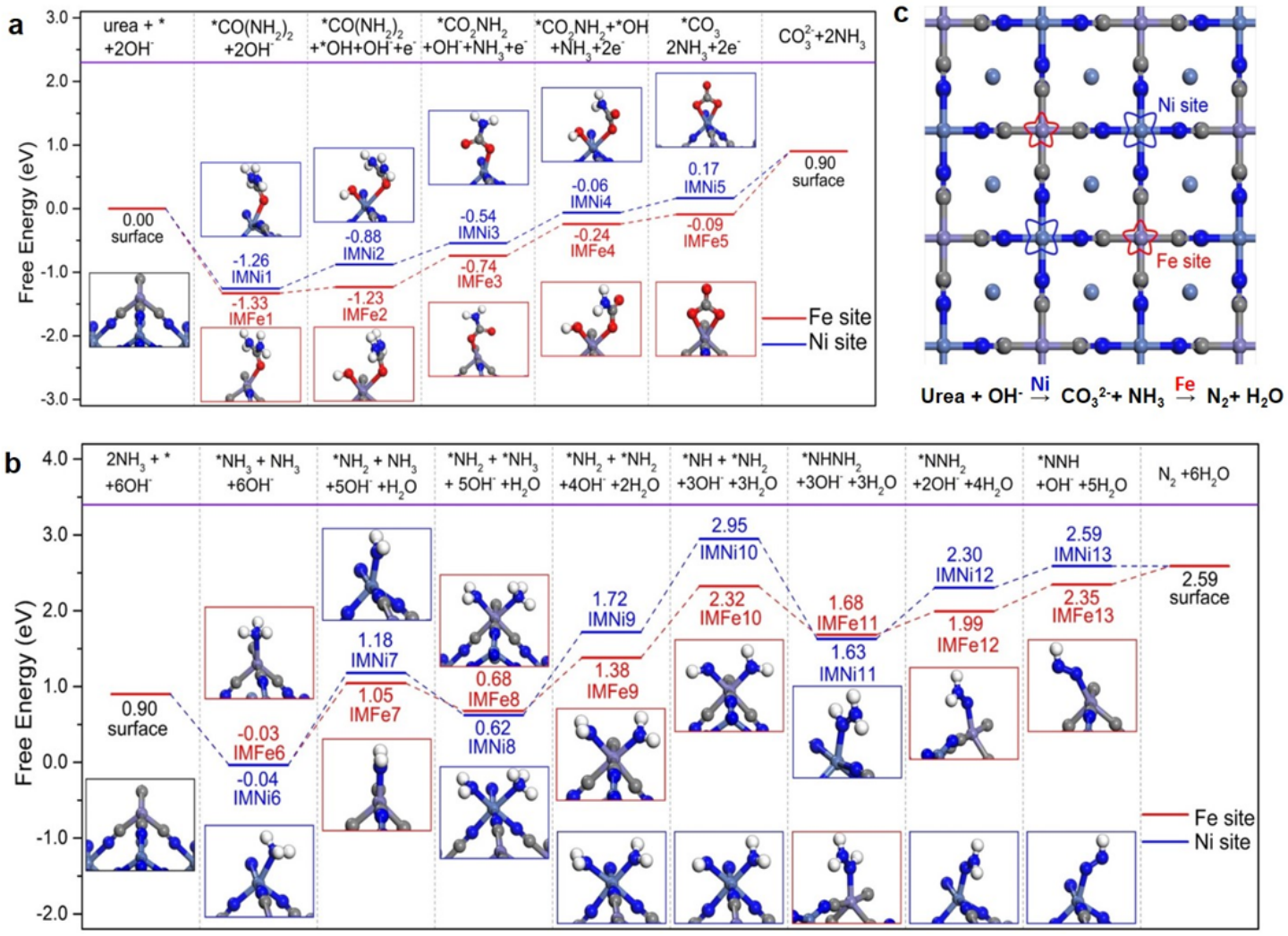

Figure 4

DFT computations. a,b, The Gibbs free energy diagrams of two step UOR (i.e., production of NH3 in panel a and oxidation of NH3 in panel b) on both Fe and Ni sites of Ni2Fe(CN)6 catalyst. Insets show the adsorption configurations of each intermediate on Fe and Ni sites and the corresponding adsorption free energies. For the first step (production of NH3), the free energy value of RDS ([M·OCO2]ads + 2e− → M + CO32−) on Ni site is smaller than that on Fe site, while for the second step (oxidation of NH3), the free energy value of RDS ([M·NH2·NH2]ads + OH− → [M·NH·NH2]ads + H2O + e−) on Fe site is smaller than that on Ni site. c, Schematic diagram of two step UOR on dual sites of Ni2Fe(CN)6 catalyst.

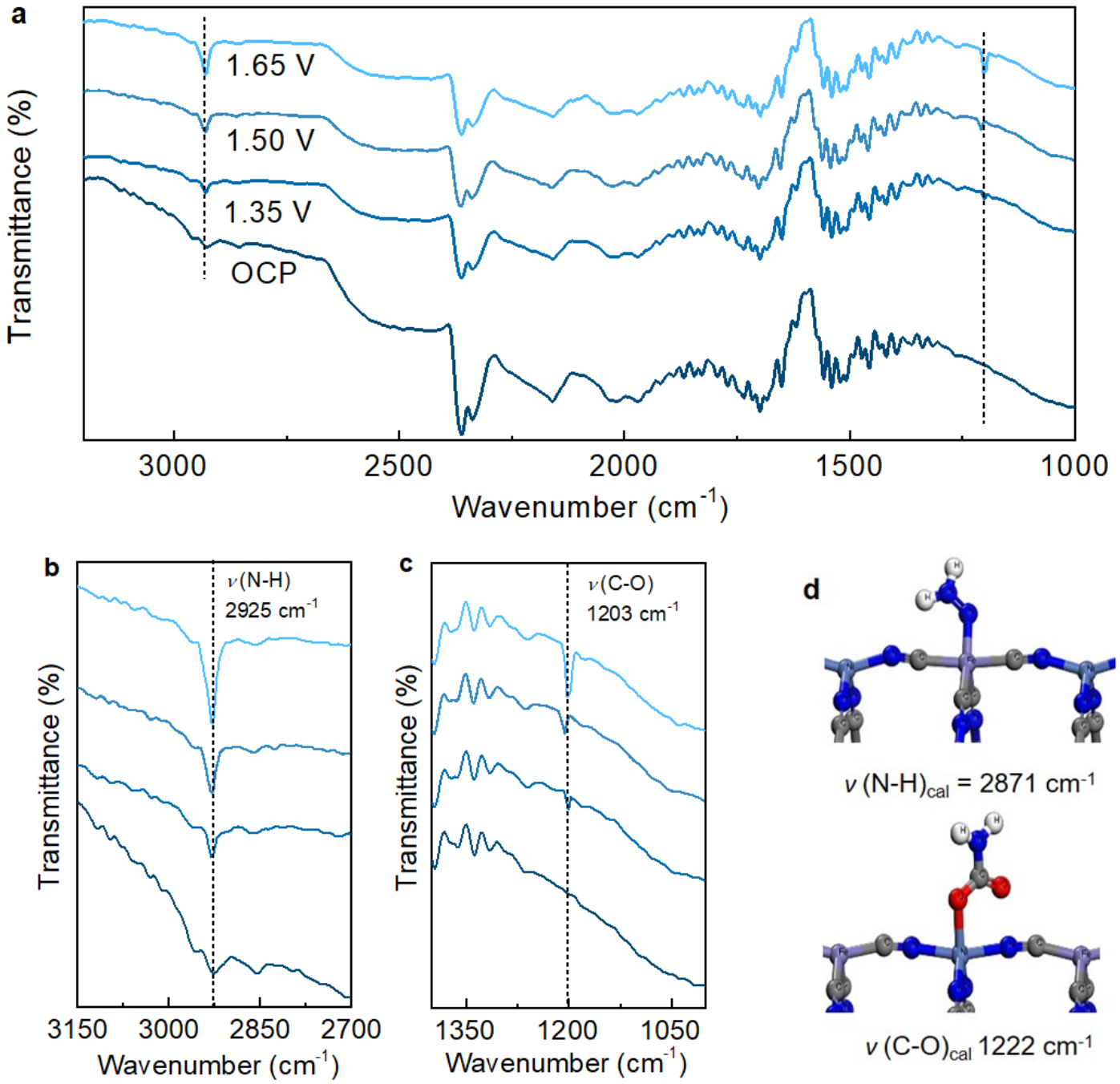

Figure 5

In-situ SR-FTIR spectra of Ni2Fe(CN)6 catalyst under different conditions. a-c, Full range and high resolution in-situ SR-FTIR spectra at different applied potentials for Ni2Fe(CN)6 catalyst. d, The calculated harmonic vibrational frequencies of N-H stretching vibration in *N=NH2+ intermediate and C-O stretching vibration in *OCONH2 intermediate on Fe and Ni adsorption sites, respectively.

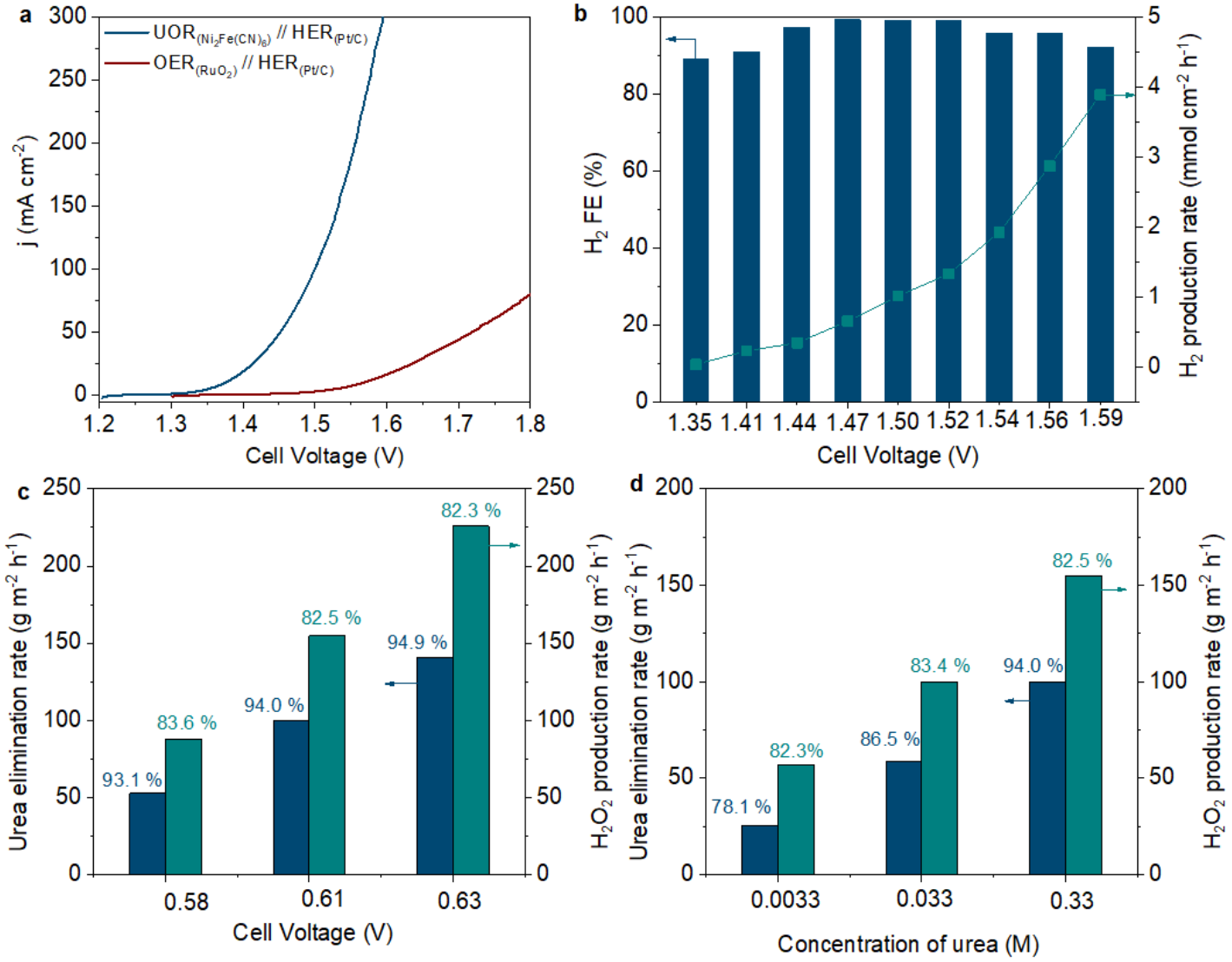

Figure 6

OER replacement by UOR in energy-saving systems for H2 and H2O2 generation. a, Comparison of LSVs for UOR//HER and OER//HER cells for different catalysts. b, Production rate and Faradaic efficiency of H2 in the UOR//HER cell at different cell voltages. c, Urea elimination and H2O2 production rates and the corresponding Faradaic efficiencies (values on the top of bars) for Ni2Fe(CN)6 catalyst in 1.0 M KOH with 0.33 M urea at different flow cell voltages. d, Urea elimination and H2O2 production rates and the corresponding Faradaic efficiencies (values on the top of bars) for Ni2Fe(CN)6 catalyst at a constant flow cell voltage of 0.61 V in 1.0 M KOH with different urea concentrations.

Supplementary Files

This is a list of supplementary files associated with this preprint. Click to download.

- UORSIsubmitted.docx